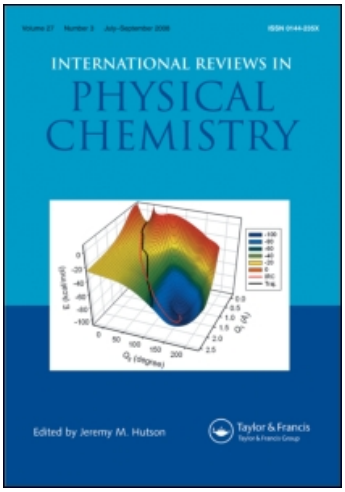

International Reviews in Physical Chemistry
Publication details, including instructions for authors and subscription information:
http://www.informaworld.com/smpp/title~content=t713724383

Infrared spectroscopy of chemically doped solid parahydrogen

Kazuki Yoshioka[a]; Paul L. Raston[a]; David T. Anderson[a]
[a] Department of Chemistry, University of Wyoming, Laramie, WY 82071-3838, USA

To cite this Article Yoshioka, Kazuki , Raston, Paul L. and Anderson, David T.(2006) 'Infrared spectroscopy of chemically doped solid parahydrogen', International Reviews in Physical Chemistry, 25: 3, 469 — 496
To link to this Article: DOI: 10.1080/01442350600802766
URL: http://dx.doi.org/10.1080/01442350600802766

International Reviews in Physical Chemistry,
Vol. 25, No. 3, July–September 2006, 469–496

Taylor & Francis
Taylor & Francis Group

Infrared spectroscopy of chemically doped solid parahydrogen

KAZUKI YOSHIOKA†, PAUL L. RASTON and DAVID T. ANDERSON*

Department of Chemistry, University of Wyoming,
Laramie, WY 82071-3838, USA

(*Received 4 April 2006; in final form 12 May 2006*)

This review article presents an overview of recent infrared spectroscopic studies of chemical species trapped in solid parahydrogen at liquid helium temperatures. An overriding theme that emerges from this work is that, even at liquid helium temperatures, chemically doped solid parahydrogen is dynamic with a variety of quantum mechanical and energy transfer processes that occur, such as orthohydrogen quantum diffusion, hydrogen nuclear spin conversion, and, in radical doped parahydrogen solids, chemical reactions can occur. To illustrate these dynamical phenomena we examine (1) clustering of orthohydrogen to dopant molecules, (2) solid parahydrogen infrared absorptions induced or perturbed by the presence of the dopant, and (3) chemical reactions initiated by infrared absorptions of the parahydrogen solid.

Contents

*Corresponding author. Email: danderso@uwyo.edu
†Present address: Department of Chemistry, University of California, 516 Rowland Hall, Irvine, CA 92697-2025, USA.

International Reviews in Physical Chemistry
ISSN 0144–235x print/ISSN 1366–591X online
http://www.tandf.co.uk/journals
DOI: 10.1080/01442350600802766

1. Introduction

The general theory of the infrared (IR) spectrum of cryogenic solid hydrogen was developed by Van Kranendonk [1–3], beginning in the late 1950s. The original infrared spectroscopy of solid hydrogen performed by Welsh and coworkers [4–8] revealed a number of unexpected condensed phase phenomena that were later made intelligible by the theoretical work of Van Kranendonk for this, the simplest of molecular solids. The infrared spectrum of solid hydrogen is purely an induced spectrum arising from the dipole moments caused by the intermolecular forces within pairs of interacting molecules and unlike the Raman spectrum vanishes when the molecules are not in close proximity to one another. Solid molecular hydrogen is like no other condensed phase due to the light mass of the H_2 molecule and the weak intermolecular forces between pairs of H_2 molecules. A full discussion of the infrared spectroscopy of solid molecular hydrogen is beyond the scope of this article and the interested reader is referred to some of the standard solid hydrogen texts [9–12] and to more recent review articles by Silvera [13] about the quantum mechanical nature of solid hydrogen, by Oka [14] on the high-resolution spectroscopy of solid hydrogen, and by Momose [15] on chemical reactions in solid hydrogen.

The use of solid molecular hydrogen as a host for matrix isolation spectroscopy is a more recent development. After Oka [14] first demonstrated in the 1980s that high-resolution ($\Delta\nu/\nu < 10^{-6}$) infrared spectroscopy is possible in solid hydrogen enriched in the *para* nuclear spin state, Momose and Shida [16] started research on the application of solid parahydrogen (pH_2) as a matrix host for the infrared spectroscopy of embedded molecules. Momose and coworkers [15] found that the infrared transitions of methane (both CH_4 and CD_4) embedded in solid parahydrogen show surprisingly sharp linewidths, indicating the methane is in well-quantized rotation–vibration states. The weak dopant–host interactions reduce the occurrence and importance of trapping site inhomogeneities, resulting in the observed sharp absorption linewidths. The correspondingly reduced cage effect in solid pH_2 allows for more efficient production of novel chemical species *via in situ* photolysis and suggests a myriad of possibilities for studying condensed phase chemical processes in a minimally perturbing environment. Furthermore, foreign dopant species induce weak but measurable IR activity in the neighboring pH_2 molecules; thus, in addition to the direct IR absorptions of the dopant, a single IR spectrum contains information about the response of the pH_2 matrix as well.

The use of solid pH_2 as a host for matrix isolation studies relies on the ability to grow transparent solid pH_2 crystals doped with chemical species that are suitable for direct absorption spectroscopy. The relatively high vapor pressure of H_2 even at liquid helium temperatures [11] prevents standard matrix isolation deposition techniques from being employed. Momose and coworkers [16] utilize condensation of a flow of a gaseous mixture containing pH_2 and the guest species in an enclosed cell maintained at 7–8 K to form crystalline pH_2 solids of length 10 cm within 2 h. Fajardo and Tam [17, 18] developed a technique they termed 'rapid vapor deposition' in which a large flow (200–300 mmol h^{-1}) of pre-cooled pH_2 gas is condensed onto a target substrate maintained at 2 K within a sample-in-vacuum liquid helium bath cryostat enabling millimeters thick pH_2 solids to be grown in less than an hour. Lee and coworkers [19] developed

a pulsed-deposition technique that can operate at deposition temperatures up to 5.5 K. The availability of new commercial closed-cycle refrigerators capable of cooling a sample target below 4 K now permits researchers [20] to utilize conventional continuous flow deposition at flow rates up to 30 mmol h^{-1}. Andrews [21] sublimes pH_2 directly onto a substrate maintained at <5 K with one of these new closed-cycle refrigerators in an experimental setup allowing for laser-ablated species to be deposited in the pH_2 solid. Nelander and coworkers [22] utilize conventional continuous flow deposition of separate gas streams of dopant and pH_2 onto a substrate maintained at 3.6 K in a small immersion helium cryostat modified for matrix work. All these various methods have there strengths and weaknesses, but the level of recent activity underscores the desire of many researchers to use solid pH_2 as a matrix host.

In solid hydrogen, the individual molecules retain good vibrational and rotational quantum numbers (v, J) because the rovibrational coupling terms in the intermolecular potential are much smaller than the rotational and vibrational energy level spacings of the individual molecules [13]. The IR absorption spectrum of solid pH_2, thus, exhibits several features that correlate with definite molecular rovibrational transitions. However, the weak intermolecular forces between two pH_2 molecules depends on the intramolecular stretching coordinate of the two molecules and, thus, leads to a mechanism for vibrational coupling. This vibrational coupling delocalizes the $v=1$ vibrational state such that the vibrational excitation can 'hop' from pH_2 molecule to pH_2 molecule within the crystal. The $v=1$ pH_2 vibrational state is broadened into a vibrational exciton band which extends over approximately 4 cm^{-1}. The exciton is termed a vibron [10]. These vibrational bands of the solid can be probed in doped pH_2 solids *via* the $Q_1(0)$ transition that corresponds to a pure vibrational transition of a pH_2 molecule and is induced by the presence of the impurity. Furthermore, if reactive species can be stabilized in solid pH_2 at liquid helium temperatures, these vibrational energy bands of the solid may provide a mechanism to induce reactions.

Solid pH_2 can be prepared with controlled amounts of orthohydrogen (oH_2) since hydrogen *ortho–para* (*o–p*) nuclear spin conversion in the cryogenic solid phase is very slow [13]. This allows solid pH_2 to be prepared at liquid helium temperatures with controlled amounts of metastable oH_2 molecules. By introducing a dopant molecule into the pH_2 solid containing low concentrations of oH_2, the dopants significantly different interactions with pH_2 and oH_2 can be studied in the pH_2 solid. In general, dopant species feel greater long-range attractive forces towards oH_2 owing to the electric quadrupole moment of hydrogen that persists in the $J=1$ rotational species (oH_2) but is averaged to zero in $J=0$ rotational species (pH_2). The stronger attraction of dopant species to oH_2 can result in preferential solvation of dopant by oH_2.

The rest of this article is organized as follows. Section 2 describes the experimental methods used in this laboratory to grow and characterize pH_2 solids doped with chemical species. In section 3, we present IR spectroscopic results on the formation of weakly bound clusters that take advantage of some of the special properties of solid pH_2. In section 4, data are presented for rare gas atom doped solid pH_2 that allows the vibrational bands of the quantum solid to be probed *via* the linewidths of the $Q_1(0)$ and $S_1(0)$ pH_2 transitions. Finally, in section 5, results are presented for infrared induced reaction of Cl atoms trapped in the pH_2 solid.

2. Experimental method

This section presents a concise summary of the experimental apparatus used to synthesize chemically doped pH_2 solids and characterize them using high-resolution Fourier transform infrared (FTIR) spectroscopy; the reader is referred to previous publications for a more detailed description [23, 24]. Parahydrogen crystals containing low concentrations of dopant species are prepared using the rapid vapor deposition technique developed by Fajardo and Tam [17, 18]. Preparation of the solid involves codeposition of independent gas flows of pH_2 and dopant onto a BaF_2 substrate maintained at $\sim$2.5 K within a sample-in-vacuum liquid helium bath cryostat. A 180-l s^{-1} turbomolecular pump is directly mounted to the base of the vacuum shroud surrounding the deposition substrate to maintain thermal isolation vacuum ($<10^{-4}$ Torr) during sample deposition. The pH_2 flow rate can be varied between 200 and 300 mmol h^{-1} allowing 3-mm thick chemically doped pH_2 crystals to be grown in about an hour.

Almost pure pH_2 gas is prepared on the fly during deposition by passing room temperature normal H_2 (nH_2) gas through a variable temperature *ortho*/*para* (*o*/*p*) catalytic converter containing granular hydrous ferric oxide ($Fe(OH)_3$). To achieve low oH_2 concentrations, the catalytic converter is maintained at 15 K, just above the 13.8 K triple point temperature of H_2, by a separate closed-cycle helium cryostat to produce 99.99% pure pH_2 solids. However, the catalytic converter can purposely be run at elevated temperatures to produce pH_2 solids with higher oH_2 concentrations. Samples thickness is determined from the integrated intensity of the $Q_1(0)+S_0(0)$ or $S_1(0)+S_0(0)$ solid pH_2 'double' IR transitions using the empirical calibration determined by Tam and Fajardo [25]. The oH_2 concentration is estimated from the measured temperature of the catalytic converter during deposition and the known thermal equilibrium concentrations of oH_2 and pH_2 as a function of temperature [13]. At low oH_2 concentrations (<0.2%), the estimated values can be checked with measured values using the integrated absorption of the $Q_1(0)$ feature at 4153 cm^{-1} and are found to be in good agreement [18, 23, 26, 27]. The flow rate of dopant is adjusted to achieve dopant concentrations in the range between 1 and 1000 parts per million (ppm) depending on the experiment. As deposited samples using this deposition method are known to contain mixed hexagonal close-packed and face centered cubic crystal domains [28]. Annealed spectra are produced by raising the temperature of the substrate to 4.4 K for a specified period of time. The temperature range from 1.8 to 4.8 K is achieved by changing the pressure above the liquid helium in the bath cryostat.

The IR absorption spectra of doped pH_2 solids are obtained with a Fourier transform infrared (FTIR) spectrometer (Bruker IFS–120HR) at maximum resolutions of 0.008 cm^{-1} (nominal with boxcar apodization). The FTIR spectrometer is equipped with glowbar or tungsten filament IR sources, Ge-coated KBr or CaF_2 beamsplitters, and liquid nitrogen cooled HgCdTe or InSb detectors. The IR probe beam is focused to approximately a 3-mm diameter spot at the sample by 90° off-axis parabolic mirrors. The entire optical path outside the spectrometer is purged with dry N_2 gas to reduce atmospheric absorptions.

The 355-nm output of a 10-Hz Nd:YAG laser (Spectra Physics Lab–170–10) is used for the *in situ* photolysis of dopants. The unfocussed 8-mm diameter Gaussian

ultraviolet (UV) laser beam with a pulse energy adjusted from 1 to 10 mJ pulse^{-1} impinges on the crystal at 45° with respect to the surface normal of the BaF_2 substrate, while the IR probe beam is directed along the surface normal. The UV laser pulse energy is measured with a power meter just before it passes through a CaF_2 window on the vacuum shroud of the cryostat. The IR probe beam comes to a focus within the region irradiated by the 355-nm laser to ensure the IR beam probes the irradiated sample area. Typically, the FTIR beam is turned off or blocked during UV laser irradiation.

3. Weakly bound clusters in solid pH_2

Some of the first results from this laboratory revealed the importance that residual oH_2 can play in the high-resolution infrared spectroscopy of chemical dopants in solid pH_2 [23]. With the current apparatus the lowest oH_2 concentration that can routinely be achieved is approximately 0.01%. Even at these low oH_2 concentrations, many times the effects of oH_2 clustering around the chemical dopant can be spectroscopically observed. This is primarily because oH_2 is mobile in solid pH_2 even at liquid helium temperatures by a rather unique mechanism called 'quantum diffusion' [29–34]. The term 'quantum diffusion' is used to describe the diffusional motion of oH_2 impurity molecules through solid pH_2 at a rate many times more rapid than can be explained by classical thermal diffusion. In general, two mechanisms have been considered quantum diffusion: (1) exchange of the nuclear spin angular momentum (I) between nearest neighbor oH_2 ($I=1$) and pH_2 ($I=0$) molecules resulting in the apparent motion of the oH_2 impurity and (2) the physical exchange in the position of nearest neighbor molecules. In the case of oH_2 quantum diffusion, the nuclear spin exchange mechanism is much faster than position exchange but for impurities, such as D_2 and HD, the position exchange mechanism is important.

3.1. *Forming weakly bound clusters*

In the case of methyl fluoride (CH_3F), the effects of oH_2 clustering are beautifully spectroscopically resolved in the infrared region using the v_3 C–F stretching vibration. The end-over-end rotational motion of CH_3F is quenched in solid pH_2 [23, 24]. Thus, the non-rotating permanent dipole moment (1.8585 D) of CH_3F [35] can interact with the quadrupole moment of the $J=1$ oH_2 molecules, while this dipole–quadrupole electrostatic interaction in not operative with the $J=0$ pH_2 molecules. The slightly greater attractive interaction of CH_3F with the $J=1$ oH_2 molecules that results from this electrostatic interaction provides the thermodynamic driving force for clustering of oH_2 molecules to the CH_3F dopant in solid pH_2. Interestingly, the addition of a single oH_2 molecule to the first solvation shell of CH_3F produces a shift in the v_3 mode of this chromophore that is readily detected using high-resolution infrared spectroscopy.

The evolution of the $CH_3F(oH_2)_n$ cluster spectra in solid pH_2 as a function of the oH_2 concentration in the crystal is shown in figure 1 for oH_2 concentrations ranging from 0.01% in trace (a) to 50% in trace (f). All spectra were recorded for samples at 2.3 K immediately after annealing the sample at 4.4 K for 5 min. Previous experiments have

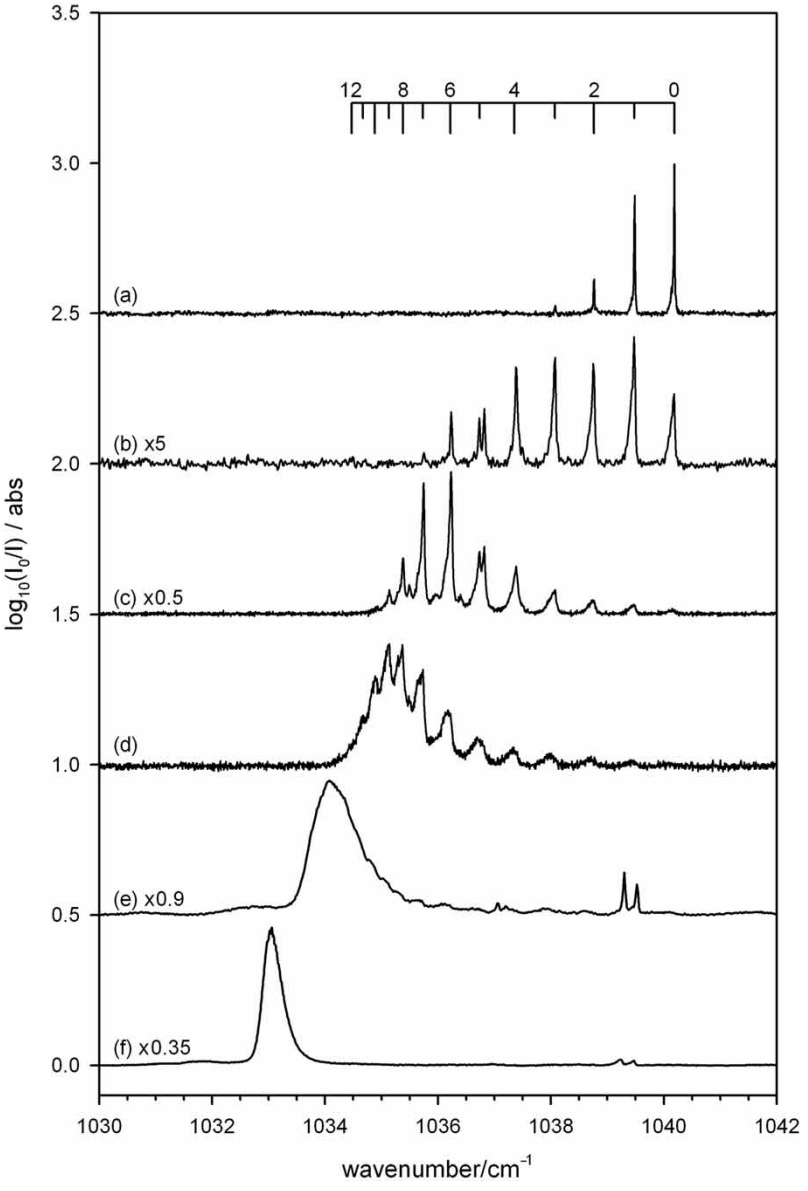

Figure 1. A series of IR absorption spectra for CH_3F-doped pH_2 crystals showing the effect of the oH_2 concentration on the measured spectrum. Spectra are in the ν_3 region of CH_3F for annealed samples recorded at 2.3 K. The oH_2 concentration in each sample is as follows: (a) 0.01%, (b) 0.22%, (c) 0.72%, (d) 1.7%, (e) 5.7% and (f) 50%. The $CH_3F(oH_2)_n$ cluster vibrational frequencies determined previously are shown on the scale at the top, labeled by the cluster size n. See text for details.

demonstrated that the multiple peak structure is due to clustering of oH_2 molecules to the CH_3F dopant [23, 24]. Each oH_2 molecule that clusters to the CH_3F shifts the ν_3 transition frequency to lower energy. These $CH_3F(oH_2)_n$ clusters irreversibly form during deposition and upon first annealing the as-deposited sample. The $CH_3F(oH_2)_n$

cluster frequencies are shown on the scale at the top of figure 1, labeled by n, the number of oH_2 molecules in the cluster. As shown in trace (a) of figure 1, even at the lowest oH_2 concentration studied, oH_2 cluster peaks are observed. Upon increasing the oH_2 concentration to 0.22% in trace (b), the cluster distribution shifts substantially towards larger clusters. Once the oH_2 concentration reaches around 1.7% in trace (d), the first solvation shell around the CH_3F is complete ($n=12$) and the resolution of individual cluster features is beginning to degrade. Note also that some cluster sizes, for example $n=5$, show multiple peak structures possibly indicating the presence of different low energy conformations for this cluster size.

Increasing the oH_2 concentration to 5.7% in trace (e) shifts the distribution to even larger clusters sizes. However, the shift in the CH_3F ν_3 transition is much less for clusters larger than $n=12$ since the oH_2 molecules now must fill the second solvation shell around the CH_3F. The dominant intermolecular interaction responsible for perturbing the ν_3 vibrational frequency [23] is an electrostatic dipole–quadrupole interaction, which falls off as R^{-4}. Even the oH_2 molecules in the second solvation shell are at significantly greater distances (5.36 Å compared to 3.79 Å) from the CH_3F chromophore and, thus, the shift per oH_2 molecule decreases significantly after the first solvation shell is filled. In these larger clusters, the individual cluster sizes can no longer be spectroscopically resolved, but rather the spectrum collapses into a single broad absorption feature whose absorption maximum is slightly to lower wavenumbers than the $n=12$ peak.

For the spectrum shown in trace (f) of figure 1, the o/p catalytic converter was run at 80 K to produce a sample that contains 50% oH_2. The peak maximum is further shifted to the red and is sharper than the peak in trace (e) at 5.7% oH_2. In the 50% oH_2 sample, all the CH_3F is solvated in large oH_2 crystalline domains since the peak maxima shifts to 1033.1 cm^{-1}. Given that the dipole–quadrupole interaction dominates the shift, we estimate that the CH_3F is sensitive to oH_2 molecules within a 10-Å radius, which translates to approximately 150 oH_2 molecules in a hexagonal close-packed pH_2 crystal lattice. Note that the absorption feature is asymmetric. This is expected as the limiting red shift value is achieved in the largest $CH_3F(oH_2)_n$ clusters. Raising the oH_2 concentration further should not result in greater red shifts, but the feature may become sharper as the 100% oH_2 concentration limit is approached.

The effects of residual oH_2 clustering are evident in the IR spectra of all the methyl halides studied in solid pH_2. A series of spectra in the region of the ν_3 C–X ($X=$ F, Cl, Br) stretching mode recorded for annealed pH_2 solids containing CH_3F, CH_3Cl and CH_3Br are shown in figure 2. All three spectra show evidence of oH_2 clustering for samples with oH_2 concentrations in the range from 0.01 to 0.03%. The simple isotopic pattern in the spectra of CH_3Cl and CH_3Br are consistent with the carrier of these signals containing only one CH_3X. The multiple peak structure in these spectra could erroneously be assigned to rotational fine structure, but analogous oH_2 concentration studies of CH_3Cl and CH_3Br reveal the multiple peak structure is due to oH_2 clustering. Based on these measurements, oH_2 clustering should be considered whenever the dopant species has a large dipole moment and, thus, preferential solvation by oH_2 is possible. The dopant can serve as an energetic trap for the oH_2 molecules present in the crystal and sequester them around the dopant. Spectroscopic studies of CO_2 and H_2O also show the effects of clustering with oH_2 [36–38].

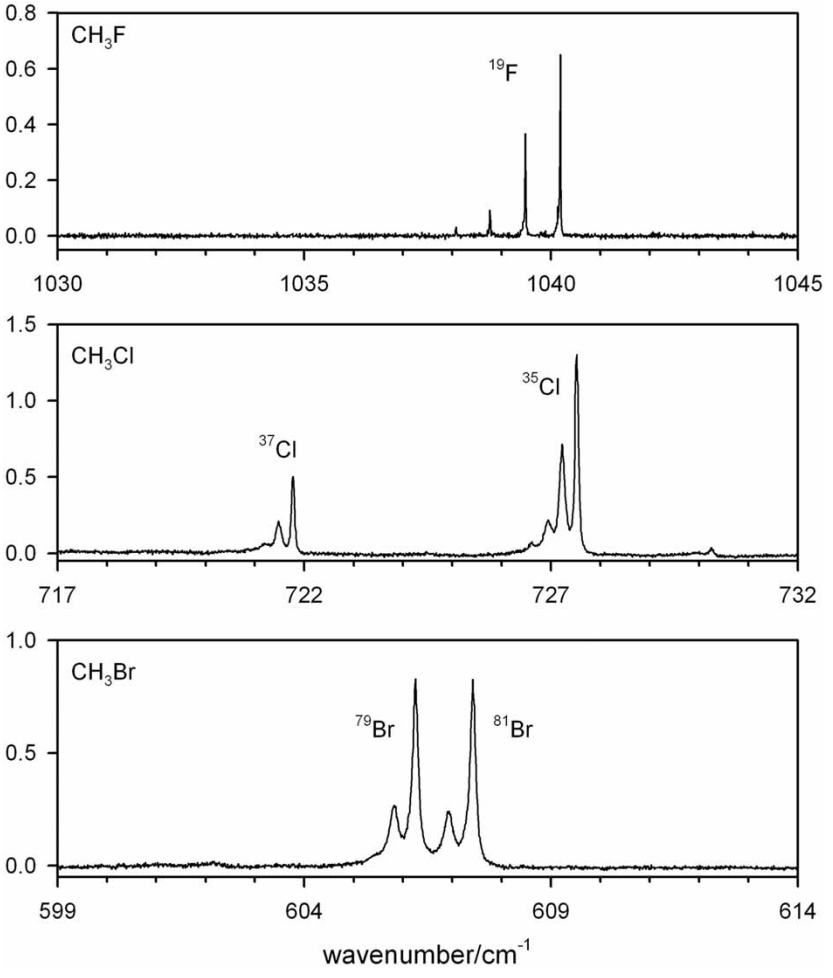

Figure 2. Infrared absorption spectra for the methyl halides CH_3X ($X = F, Cl, Br$) trapped in solid pH_2, illustrating the common phenomena of clustering with residual oH_2. Spectra are in the methyl halide ν_3 region and the oH_2 concentration is in the range between 100 and 300 ppm. The concentrations of methyl halide in the spectra are 0.4 ppm CH_3F, 41 ppm CH_3Cl, and 150 ppm CH_3Br.

Continuation of these cluster studies led us to investigate the infrared spectroscopy of the clusters $N_2O(oH_2)_n$, $N_2O(oD_2)$, and $N_2O(HD)_n$ in solid pH_2. These studies were motivated primarily by the eloquent IR spectroscopic studies of these clusters in pulsed supersonic expansions by McKellar and coworkers [39, 40]. Analogous spectroscopic studies of ^4He_n-N_2O clusters by Jäger and McKellar [41] have extended previous helium nanodroplet isolation spectroscopy results [42, 43] which involved cluster sizes of $n \approx 10^3$–10^4 to the regime of small clusters with $n \approx 2$–20. In a similar vein, we have investigated N_2O–hydrogen clusters solvated in solid pH_2 to compare our spectroscopic results with the data for finite sized clusters in the gas-phase [44]. Clusters of molecular hydrogen have attracted considerable experimental [45–47] and theoretical [48–50] attention owing to their highly quantum mechanical nature. In particular, pH_2 clusters

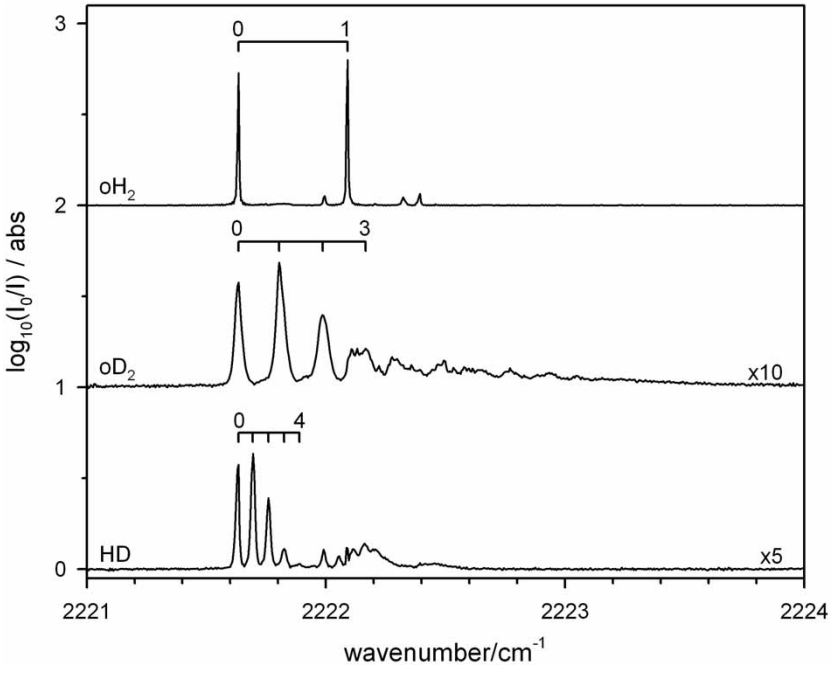

Figure 3. Infrared spectra in the v_3N–N stretch region of $N_2O(oH_2)_n$, $N_2O(oD_2)_n$ and $N_2O(HD)_n$ clusters trapped in solid pH_2 and recorded at 4.33, 4.39 and 4.66 K, respectively. In each case the cluster spectra are labeled by n, the number of hydrogen species in the cluster.

are considered potential candidates for the detection of a new superfluid phase of molecule hydrogen. In terms of quantum solvation, Moore and Miller [51–55] studied small hydrogen clusters such as $(H_2)_n$–HF and HCN–$(HD)_n$ embedded in helium nanodroplets, observing remarkable size-dependent effects on the rotational dynamics of the dopant molecule. The IR spectra of the N_2O–hydrogen clusters solvated in solid pH_2 where the cluster is confined to the solvent cavity of bulk solid pH_2, therefore, provide an interesting point of comparison with the finite size gas-phase cluster studies and studies conducted in helium nanodroplets.

The $N_2O(oH_2)_n$, $N_2O(oD_2)_n$, and $N_2O(HD)_n$ cluster spectra demonstrate the subtle vibrational shifts that can be resolved in solid pH_2 [44]. A series of IR spectra in the v_3 region of N_2O for solid pH_2 crystals co-doped with N_2O ($\sim$1 ppm) and oH_2 (0.1%), oD_2 (50%) or HD (50%) are presented in figure 3. Similar to figure 1, the scale at the top of each spectrum indicates n, the number of hydrogen species in the cluster. For example, the shift indicated in the top trace of figure 3 corresponds to the difference in the v_3 vibrational frequency (N–N stretch) of N_2O caused by replacing one of the pH_2 molecules in the first solvation shell of N_2O with an oH_2. The presence of one oH_2 molecule ($n=1$) in the first solvation shell of N_2O shifts the v_3 vibrational frequency $+0.457\,cm^{-1}$ to higher energy. The observed blue shift correlates well with the difference between the vibrational origins of the N_2O–oH_2 and N_2O–pH_2 van der Waal's dimers measured by McKellar and coworkers [39]. These data are compared in table 1.

Table 1. Comparison of gas-phase van der Waal's dimer vibrational origin differences ($\nu_0^X - \nu_0^{pH_2}$) and solid pH_2 ($n=1-n=0$) cluster shifts. All values in cm^{-1}.

Species	Gas-phase[a]	Solid pH_2	Difference
ortho-H_2	+0.3977	+0.457	−0.059
ortho-D_2	+0.2273	+0.172	+0.055
HD	+0.0919	+0.062	+0.030

[a] From [39].

Similar to the $CH_3F(oH_2)_n$ cluster studies, the small shift indicates that pH_2 and oH_2 interact differently with N_2O in solid pH_2. While both nuclear spin isomers of H_2 interact with N_2O on the same Born–Oppenheimer intermolecular potential energy surface, because the H_2 rotational quantum number is conserved in solid pH_2, the interaction potential is averaged over either a $J=1$ or $J=0$ H_2 rotational wavefunction for oH_2 and pH_2, respectively. When the interaction is averaged over a $J=0$ rotational state, all anisotropic interactions average to zero. In contrast, the anisotropic interactions survive averaging over a $J=1$ rotational state and, thus, $J=1$ oH_2 has an effective quadrupole moment. The $+0.457\,cm^{-1}$ shift caused by a single oH_2 molecule in the first solvation shell of N_2O is easily resolved in solid pH_2 because the linewidths of the absorptions are in the order of $0.01\,cm^{-1}$.

Even more amazing are the small shifts measured for orthodeuterium (oD_2) and HD. In these cases, the interaction does not differ because of averaging over a $J=1$ rotational wavefunction as was the case for oH_2. Both oD_2 and HD are presumed to be in their ground $J=0$ rotational state at these temperatures similar to pH_2. Thus, the $+0.172$ and $+0.063\,cm^{-1}$ blue shifts are caused by the small mass difference between these species and H_2, which results in reduced translational zero-point motion. Even at $T=0\,K$, the H_2 molecules are not sharply localized at lattice sites due to large amplitude zero-point motion; in solid pH_2 the root mean square (rms) width of the single particle distribution function is ~18% of the nearest neighbor distance [13]. This large zero-point motion is a result of the weak isotropic intermolecular forces between pairs of pH_2 molecules and the light mass of H_2. Thus, the heavier oD_2 and HD will have a reduced radial zero-point motion with respect to the heavy N_2O and sit closer on average to N_2O than pH_2 causing the observed shifts. Indeed, the $n=1$ to $n=0$ shifts measured in solid pH_2 correlate well with the differences in the vibrational band origins measured by McKellar [39] for the corresponding isolated van der Waal's dimers (see table 1).

The $N_2O(oH_2)_n$ clusters were prepared in the same way as the $CH_3F(oH_2)_n$ clusters were formed, by thermally annealing the sample at 4.4 K for a specified period of time. Even crystals grown with 100 ppm oH_2 concentrations show spectroscopic evidence of $N_2O(oH_2)_n$ cluster formation due to facile quantum diffusion of oH_2 in solid pH_2. However, N_2O clusters with oD_2 and HD do not form under similar conditions since the quantum diffusion of D_2 and HD is much slower than oH_2 diffusion. Thus, to make clusters of N_2O with D_2 and HD we made 50 : 50 mixtures of $H_2:D_2$ or $H_2:HD$ and passed these gas mixtures through the *o*/*p* catalytic converter and co-deposited the gas mixture with N_2O. Similar hydrogen cluster studies of OCS in solid pH_2 have been conducted and will be reported elsewhere.

3.2. *Intracluster nuclear spin conversion*

At low oH_2 concentrations (<0.2%) the $CH_3F(oH_2)_n$ cluster spectra show evidence of *o–p* conversion of oH_2 molecules within the cluster [23, 24]. Figure 4 shows IR spectra of a CH_3F-doped sample with an oH_2 concentration of ~0.01%. Trace (a) is recorded at 2.1 K for the as-deposited sample. Trace (b) is recorded at 4.4 K after annealing the sample and shows the irreversible growth of the $CH_3F(oH_2)_n$ clusters upon annealing. At this low oH_2 concentration, annealing the sample acts to sequester the trace amounts of oH_2 around the CH_3F. The temperature is reduced in trace (c) to 2.3 K with no apparent increase in cluster size. While the free oH_2 can still quantum diffuse through the solid, most of the oH_2 is already clustered to CH_3F in the annealed sample at 4.4 K, so no shift in the cluster distribution is observed upon lowering the temperature.

Instead, what is measured is a gradual shift with time in the cluster distribution to smaller cluster sizes. This process is ascribed to intracluster hydrogen *o–p* conversion and is illustrated in figure 4 where trace (d) was recorded 4.5 h after trace (c) while the sample was maintained at 2.3 K. In trace (c), clusters as large as $n=3$ are observed, while in trace (d) only the $n=1$ and $n=0$ absorptions are measurable. The rate of intracluster *o–p* conversion must be significantly greater than the growth of $CH_3F(oH_2)_n$ clusters by quantum diffusion of oH_2 at these low oH_2 concentrations

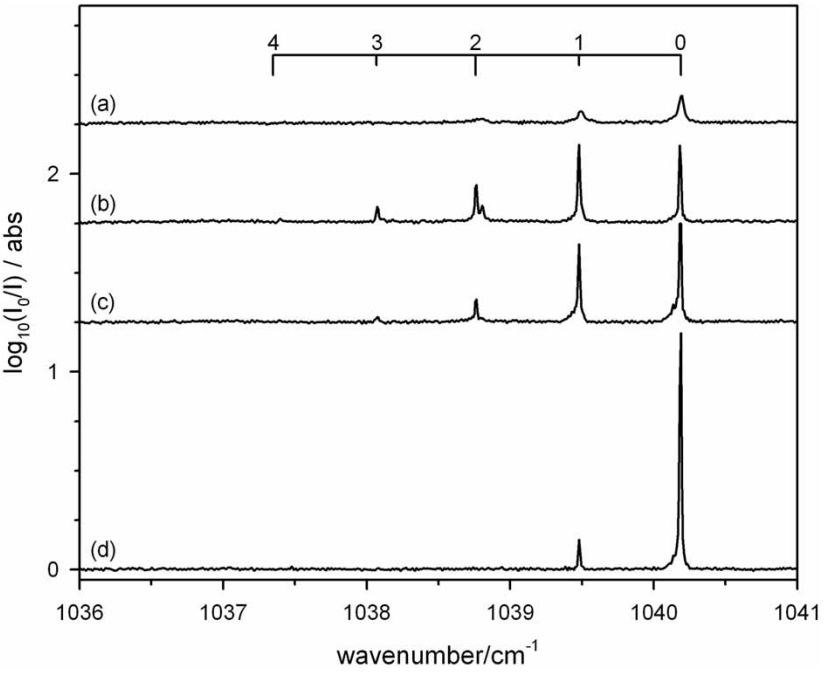

Figure 4. IR spectra of a 2-mm thick, 0.4 ppm CH_3F-doped pH_2 sample with 100 ppm oH_2 at a resolution of 0.02 cm^{-1}. Trace (a) is the as-deposited spectrum recorded at 2.1 K; trace (b) is recorded at 4.4 K for the annealed sample; trace (c) is recorded immediately after lowering the temperature to 2.3 K; trace (d) is recorded 270 min after trace (c), while maintaining the sample at 2.3 K. The cluster size n is labeled on the scale above the spectra.

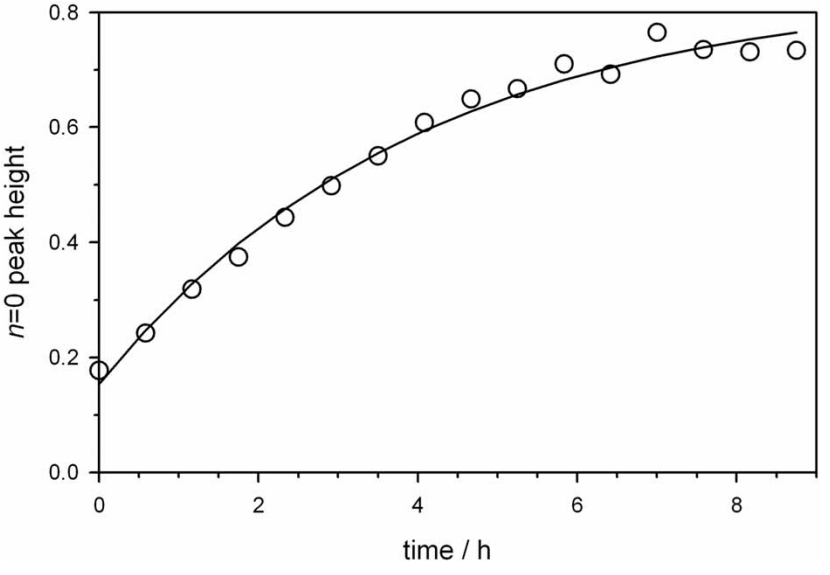

Figure 5. Peak height of the CH_3F $n=0$ absorption feature at 1049.19 cm^{-1} as a function of time for a sample maintained at 2.3 K. The solid line is the fitted exponential curve.

where, in annealed samples, most oH_2 molecules are already clustered to dopant molecules. More detailed studies of $CH_3F(oH_2)_n$ cluster growth and decay over a range of oH_2 concentrations are presented elsewhere [24].

The growth of the $n=0$ peak with time is displayed in figure 5 for a sample maintained at 2.3 K. It is important to point out that the growth of the $n=0$ peak indicates the CH_3F dopant is capable of inducing the *o–p* conversion process in the adjacent oH_2 molecules since the growth of the $n=0$ absorption corresponds to the reaction $CH_3F–oH_2 \rightarrow CH_3F–pH_2$ in isolated pairs. The growth of the $n=0$ peak is determined from the peak height of the $n=0$ feature. Since the absorption features are very sharp (0.02 cm^{-1}) there is some scatter in the data; however, the trends of the data with time are definite and have been measured in repeated experiments. The solid curve in figure 5 is the result of an equally weighted least-squares fit of the data by an equation of the form:

$$P(t) = A + B(1 - e^{-kt}) \tag{1}$$

where $P(t)$ is the peak height and t is the time after the annealed sample is cooled to 2.3 K. It should be noted that fitting the data to equation (1) is approximate since it treats the kinetic process as simply $n=1 \rightarrow n=0$, whereas in reality the process is more complicated and involves sequential first-order conversion (*i.e.* $n=3 \rightarrow 2 \rightarrow 1 \rightarrow 0$). A fit of the data shown in figure 5 to equation (1) gave a rate constant of $k=0.25(6)\,h^{-1}$, where the reported error is the two-sigma value in the fitted constant. The measured CH_3F induced rate constant is approximately 10 times larger than the self-conversion rate constant, which is $K=0.019\,h^{-1}$ [13]. The self-conversion process

occurs by the formation of oH_2–oH_2 dimers within the solid since there is no mechanism for *o–p* conversion in isolated pH_2–oH_2 pairs. The faster *o–p* conversion rate constant measured for $CH_3F(oH_2)_n$ clusters most likely reflects the fact that it measures conversion within a cluster, whereas the self-conversion rate constant is a measure of both oH_2 cluster formation and *o–p* conversion.

Soon after the discovery of the *ortho–para* nuclear spin states of hydrogen, experimental investigations showed that the rate equation governing conversion in the solid or liquid was second-order with respect to the oH_2 concentration [9, 13, 56]. For H_2, inhomogeneous magnetic fields on the molecular scale provide by far the most important conversion channel. Thus, for an oH_2 molecule to convert in the solid or the liquid, it must feel the dipolar magnetic field of another oH_2 molecule, since pH_2 ($J=0$, $I=0$) has no magnetic moment. Similar to oH_2, the CH_3F molecule exists in two nuclear spin states depending on the total nuclear spin of the three equivalent hydrogens, either $I=1/2$ (*para*) or 3/2 (*ortho*). Since the CH_3F molecule does not freely rotate in solid pH_2, the population of the two nuclear spin states can not be determined using IR spectroscopy. However, in either nuclear spin state, CH_3F has nonzero total nuclear spin that will create inhomogeneous magnetic fields around the CH_3F dopant. Furthermore, the H and F nuclei in CH_3F have large nuclear magnetic dipole moments of several nuclear magnetons. Thus, CH_3F can induce *o–p* conversion of oH_2 molecules in direct contact with the CH_3F through nuclear spin–spin interactions.

The *o–p* conversion process catalyzed by paramagnetic species, such as O_2, has been studied and is thought to convert oH_2 at much greater rates since the unpaired electron creates much larger magnetic field gradients [57]. In fact, for O_2 catalyzed *o–p* conversion, the conversion rate is much faster than the diffusion rate of oH_2 and, thus, the catalyzed conversion is considered a diffusion-controlled chemical reaction. However, in the case of CH_3F, the magnetic moment is quite small, in the order of a few nuclear magnetons and, thus, the *o–p* conversion rate is slow enough to spectroscopically observe the $CH_3F(oH_2)_n$ clusters using FTIR but fast enough to measure *o–p* conversion over the 8–10-h duration of our experiments. Indeed, annealed samples grown using the rapid vapor deposition technique [17, 18] provide a novel way to study *o–p* conversion catalyzed by closed-shell dopant molecules.

Further experiments with other methyl halides (CH_3Cl and CH_3Br) show similar *o–p* conversion rates. In contrast, species such as OCS and N_2O, which are also preferentially solvated by oH_2 in solid hydrogen, do not show the ability to induce *o–p* conversion within the cluster, at least on the timescale of our experiments. The most recent N_2O experiments indicate the presence of minor *o–p* conversion, but at much slower rates than measured for CH_3F. Similar studies of $H_2O(oH_2)_n$ clusters in solid pH_2 seem to indicate that H_2O can also induce intracluster *o–p* conversion; however, the kinetics were not studied in detail [38]. Interestingly, these researchers speculate that the nuclear spin conversion process for the oH_2 and oH_2O species are somehow linked. In our case, since the CH_3F is not freely rotating, we can not determine the effect of the nuclear spin state of CH_3F on the *o–p* conversion process. The spectroscopic detail with which these studies can be carried out should lead to new insights into how *o–p* conversion occurs in chemically doped solid hydrogen.

4. Dopant-induced IR activity

Our group in collaboration with Fajardo and Hinde has been studying solid pH_2 IR absorptions induced by the presence of a chemical impurity [26, 27]. The chemical impurity can polarize the pH_2 molecules adjacent to it leading to new infrared transitions. Recent work in this area has focused on infrared-active bands associated with rare gas (Rg) atom (Ne, Ar, Kr, and Xe) substitutional impurities [58, 59]. This work is aimed at (1) using the induced infrared transitions as quantitative probes of the concentration and identity of non-infrared active impurities, such as atoms, and (2) a better understanding of how the impurity perturbs the excited rovibrational states of solid hydrogen, so that we can utilize these excitations in vibrationally driven chemistry (discussed in more detail in the following section). The rare gas atoms were chosen since the intermolecular potentials with hydrogen, Rg–H_2, are well known [60, 61] and can be used in theoretical studies of these phenomena.

In this section we will explore two IR-induced absorptions in cryogenic solid pH_2 doped with Rg atoms: the $Q_1(0)$ transition at $\sim 4150\,cm^{-1}$, which corresponds to a pure vibrational transition ($v=1, J=0 \leftarrow v=0, J=0$) of a pH_2 molecule, and the $S_1(0)$ rovibrational transition ($v=1, J=2 \leftarrow v=0, J=0$) at $4486\,cm^{-1}$, which involves both vibrational and rotational excitation of a single pH_2 molecule. These two transitions have encoded in their high-resolution IR absorption lineshape information about the configuration distribution function of the Rg atoms and the surrounding pH_2 solvation shell. The ability to dope solid pH_2 with Rg atoms opens up new possibilities to study the induced IR spectrum of solid pH_2 that should extend the theoretical understanding pioneered by Van Kranendonk [1–3]. The Rg atom-doped solid pH_2 system is also amenable to first principles calculations [58] and it is hoped that the experimental data presented in this paper will motivate further theoretical work.

The $Q_1(0)$ transition in solid molecular hydrogen has been extensively studied [3, 8, 62] and is not observed in pure pH_2 crystals because, in the high symmetry environment of the hexagonal close-packed crystal lattice, the induced dipole moments in pairs of interacting pH_2 molecules tend to cancel one another. However, if the pH_2 crystal is doped with low concentrations of impurity molecules, the symmetry around the dopant is broken and the $Q_1(0)$ transition becomes observable. In the case of spherical dopants such as Rg atoms, the induction mechanism is similar to a collision-induced mechanism and originates from short-range isotropic overlap of the electron densities of the impurity and H_2 that polarize the collision pair, creating a weak transition dipole moment [58]. These short-range interactions play an especially important role in solid pH_2 due to the large amplitude zero-point motion of the individual pH_2 molecules. In addition, weak vibrational coupling between neighboring molecules in solid pH_2 results in broadening of the $v=1$, $J=0$ excited state into a vibron band, in which the vibrational excitation becomes delocalized and travels throughout the solid. The width of the vibron band is in the order of a few wavenumbers and corresponds to the strength of the vibrational coupling between nearest neighbor pairs or, in other words, the broader the band the faster the vibration 'hops' from pH_2 molecule to pH_2 molecule.

4.1. *Rg atom-induced $Q_1(0)$ vibron band*

To minimize the intensity of the oH_2 induced $Q_1(0)$ absorption feature, crystals were grown with the minimum amount of oH_2 that can be achieved, which is 100–300 ppm. Since the *o–p* conversion rate in the solid at these low oH_2 concentrations is in the order of days, all the absorption profiles presented in this section contain a small contribution from the oH_2-induced $Q_1(0)$ absorption. However, the frequency and lineshape of this absorption feature are well known and, at these oH_2 concentrations, it does not significantly mask the measured Rg atom-induced $Q_1(0)$ features.

A series of spectra in the $Q_1(0)$ region are shown in figure 6 for pH_2 crystals doped with different Rg atoms. The spectrum shown in trace (a) of figure 6 is for a pure pH_2 crystal, no Rg atom dopant, and illustrates the small oH_2-induced $Q_1(0)$ absorption feature that is present in all the spectra due to residual oH_2. Traces (b)–(e) are recorded at 2.0 K for as-deposited pH_2 samples containing Ne, Ar, Kr and Xe, respectively. Note that attempts to observe the He atom-induced $Q_1(0)$ absorption were unsuccessful, even for samples deposited with relatively high He gas flow-rates. Possible reasons for the lack of a He-induced $Q_1(0)$ feature could be the inability of the pH_2 crystals to trap

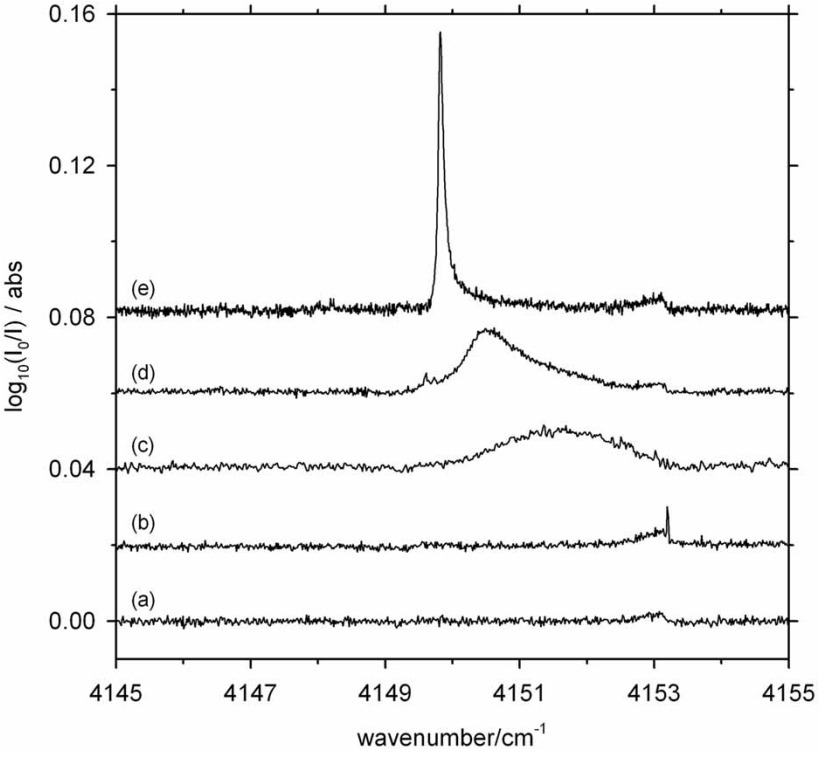

Figure 6. Infrared absorption spectra of Rg atom-doped solid pH_2 in the $Q_1(0)$ region. All samples are as-deposited and spectra are recorded at 2.0 K. Trace (a) is of a 2.8-mm thick neat pH_2 solid containing 100 ppm of residual oH_2. The other spectra are Rg atom-doped samples with Rg atom concentrations as follows: trace (b) 1000 ppm Ne, (c) 1300 ppm Ar, (d) 970 ppm Kr, and (e) 260 ppm Xe.

sufficient concentrations of He atoms and/or that the He-induced $Q_1(0)$ feature is extremely weak and below current detection limits.

Examination of figure 6 shows the trend that the Rg atom-induced $Q_1(0)$ absorption feature shifts to lower energy and narrows going from Ar to Kr to Xe. Note that Ne, however, does not follow this trend, with almost no induced signal except for possibly the sharp absorption feature right at the blue edge of the $Q_1(0)$ feature induced by residual oH_2 present in the crystal. The spectra shown in figure 6 were recorded for Rg atom concentrations of approximately 1000 ppm, except for the Xe-doped sample, which has a concentration of 260 ppm.

The vibrational frequency of pH_2 molecules in direct contact with the Rg atom in the solid are shifted to lower energy, which is known from related van der Waal's dimer studies [63, 64], and this decouples the vibrational coordinates of these pH_2 molecules from the bulk. Thus, as the $Q_1(0)$ absorption shifts to lower energy it also sharpens because the Rg atom localizes the vibron on pH_2 molecules in the first solvation shell of the Rg atom. This is the case for Xe but the vibron is more delocalized for Ar. The extent of localization of the vibron depends sensitively on how the Rg atom perturbs the energy of the $v=1$ excited state of the pH_2 molecules that solvate the Rg atom in the solid.

The magnitude of the perturbation depends on the strength of the isotropic Rg–H_2 potential and on the vibrationally averaged radial distance between the Rg atom and the pH_2 molecules. The shift in the pH_2 vibrational frequency only depends on the isotropic terms in the intermolecular potential since the $Q_1(0)$ transition involves only $J=0$ pH_2 rotational states. In the solid, the radial distance of the first solvation shell around the Rg atom is determined by a balance between the pH_2–pH_2 intermolecular interactions and the Rg–pH_2 intermolecular interactions. Based on the shift of the $Q_1(0)$ feature to lower energy, it appears that, for Ar, Kr and Xe, the dominant interaction is attractive between the Rg atom and the first solvation shell. In contrast, for Ne, the interaction with the first solvation shell is dominated by repulsive interactions and, thus, the induced $Q_1(0)$ transition does not follow the trend established by Ar, Kr and Xe. In addition, first principles calculations by Hinde [58] reproduce the trend measured for Ar, Kr and Xe nearly quantitatively. It will be interesting to see if future calculations can reproduce the Ne-induced $Q_1(0)$ feature.

4.2. *Rg atom-perturbed $S_1(0)$ transitions*

The $S_1(0)$ transition of pH_2 corresponds to the rovibrational excitation of a single pH_2 molecule [8, 65] to a $v=1$, $J=2$ excited state. Similar to the $Q_1(0)$ transition, the excited state is an exciton state; however, the bandwidth is much less and, accordingly, the linewidth of the $S_1(0)$ transition is quite sharp. The M_J degeneracy in the excited state is lifted by interactions with the surrounding pH_2 lattice, but the IR selection rules result in transitions only to the $M_J=\pm 2$ level in hexagonal close-packed (hcp) solid pH_2 [65]. The $S_1(0)$ transition is sharper than the $Q_1(0)$ transition due to the weaker coupling between $v=1$, $J=2$ and $v=0$, $J=0$ compared to the coupling between $v=1$, $J=0$ and $v=0$, $J=0$. Quite simply, since the $S_1(0)$ transition involves both rotational and vibrational excitation of a single pH_2 molecule, the terms in the intermolecular potential

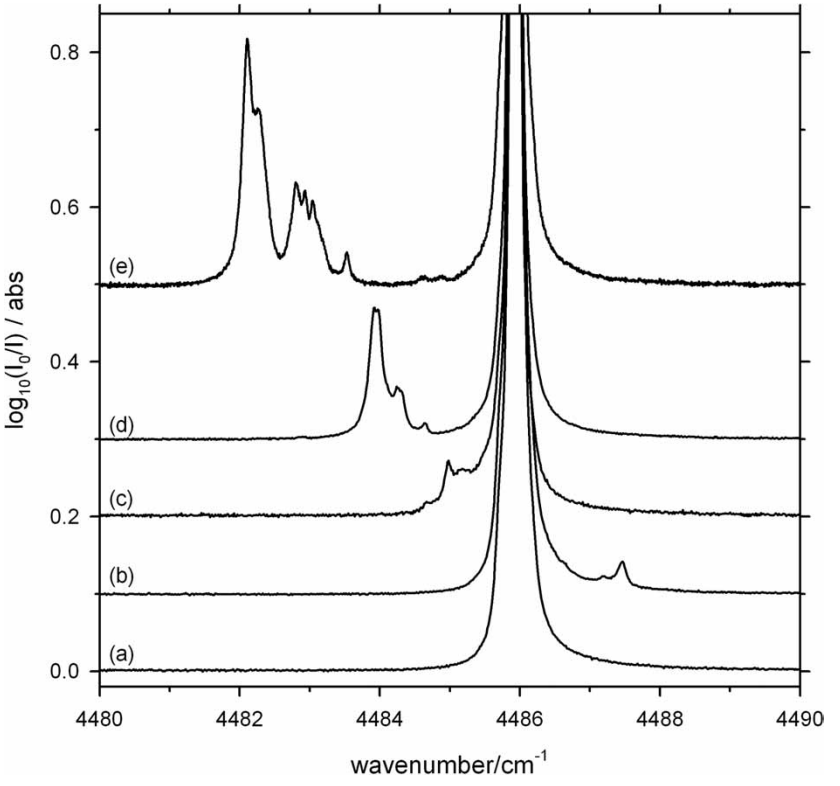

Figure 7. Infrared spectra of Rg atom-doped solid pH_2 in the $S_1(0)$ region. The samples and conditions are the same as presented in figure 6.

that couple both vibration and rotation are significantly smaller than the potential terms that involve coupling just vibrational excitation.

Figure 7 shows the $S_1(0)$ region of the Rg atom-doped pH_2 samples shown in figure 6. Trace (a) is for a pure pH_2 sample and only shows the allowed $S_1(0)$ transition with no satellites at approximately 4485.94 cm^{-1}. Similar to the $Q_1(0)$ region, there is a clear trend going from Ar to Kr to Xe. The satellite features all occur at lower energies than the $S_1(0)$ transition and progressively shift to lower energy going down the periodic table. The Xe-perturbed satellite feature shows the most structure, with at least six resolved peaks. In contrast, the Ne-perturbed satellite $S_1(0)$ transitions are at a higher energy than the $S_1(0)$ transition.

Quantitative interpretation of the lineshape of the Rg atom-perturbed $S_1(0)$ transitions shown in figure 7 awaits comparison to detailed theoretical calculations. Since the $S_1(0)$ transition accesses a $J=2$ rotational state in the upper state, the spherical nature of the pH_2 molecule is lost. The pH_2 molecule in a $J=2$ rotational state can interact with the Rg atom through both isotropic and anisotropic intermolecular forces. The anisotropy in the Rg–H_2 intermolecular potential lifts the M_J degeneracy of the $v=1$, $J=2$ pH_2 upper state. Two limiting cases of the nature of the upper exciton

state are complete delocalization of the excitation over the 12 nearest neighbor pH_2 molecules surrounding the Rg impurity or complete localization of the excitation on an isolated pH_2–Rg pair. If the excitation is completely localized on an isolated pH_2–Rg pair, then the quantization axis is along the pair axis and the transition should be split into three M_J sublevels ($M_J = \pm 2, \pm 1, 0$). Further smaller splittings would also result since there are both in-plane and out-of-plane configurations of the pair within the hcp crystal lattice [10]. If the excitation is completely delocalized over the 12 nearest neighbor pH_2 molecules, then the splitting pattern would be expected to be more complicated since now there are potentially 12 $J = 2$ pH_2 molecules with $12 \times 3 = 36$ combinations of the $M_J = \pm 2, \pm 1, 0$ levels where now the quantization axis is along the crystal axis. We speculate that the measured Rg atom perturbed $S_1(0)$ satellite features indicate that both the rotational (roton) and vibrational (vibron) excitations are delocalized over all 12 nearest neighbors since more than three peaks are resolved. Interestingly, the Ne feature is shifted to higher energy consistent with the induced $Q_1(0)$ feature and the splitting pattern in the $S_1(0)$ feature is reversed. This is consistent with the dominant interaction of the Rg atom with the first solvation shell being repulsive in the case of Ne and attractive in the cases of Ar, Kr and Xe. Clearly the present interpretations are highly speculative and we hope these experimental spectra motivate detailed quantum calculations. Only through a combination of experiment and theory will the nature of the Rg atom-perturbed $S_1(0)$ upper exciton state be revealed.

5. Infrared-induced chemical reactions

If reactive species can be stabilized in solid pH_2 at liquid helium temperatures, vibrational energy bands [1, 3, 10, 62] of the solid may provide a mechanism to induce chemical reactions of the type $X + H_2(v = 1) \rightarrow HX + H$. As discussed in the previous section, in solid pH_2, the $H_2(v = 1)$ intramolecular vibrational excitation can 'hop' from pH_2 molecule to pH_2 molecule *via* a resonant energy-coupling mechanism allowing the excitation to travel throughout the crystal [1, 3, 10, 62]. The $v = 1$ pH_2 vibrational state, or vibron, is thus broadened ($4\,cm^{-1}$) into a vibrational exciton band at $4152\,cm^{-1}$. If vibrons are created in a solid pH_2 crystal containing reactive species X, then the vibron may supply sufficient energy to induce reaction such that the reaction proceeds at a measurable rate even while the solid is maintained at liquid helium temperatures.

The present work focuses on using 355-nm photodissociation of Cl_2 embedded in solid pH_2 to create pH_2 solids doped with $\sim$100 ppm concentrations of Cl atoms. The reaction:

$$Cl(^2P_{3/2}) + H_2(v = 0) \rightarrow HCl + H \tag{2}$$

is endothermic by $360\,cm^{-1}$ and, thus, ground spin–orbit state Cl in solid pH_2 at liquid helium temperatures should be remarkably stable [66]. Reaction (2) can not proceed, even *via* quantum mechanical tunneling through the barrier, since the

products are 360 cm^{-1} higher in energy. In contrast, the reaction with vibrationally excited H_2

$$Cl(^2P_{3/2}) + H_2(v = 1) \rightarrow HCl + H \quad (3)$$

is exoergic by 3800 cm^{-1} and, thus, this reaction is energetically possible. Furthermore, for reactions with late transition states, such as this reaction, vibrational excitation of the diatomic reagent is known to effectively couple to the reaction coordinate [67].

The IR-induced reaction kinetics is measured using two experimental setups: either with a 3861-cm^{-1} longpass optical filter (LPF) or a 5500-cm^{-1} LPF in the IR beam. The high energy region of the transmission spectrum under these two experimental conditions is shown in figure 8. The IR-induced reaction kinetics is measured with the 5500 cm^{-1} LPF in the IR beam, whereby there is significant IR intensity in the 4000–5000 cm^{-1} range. In contrast, with the 3861-cm^{-1} LPF in the IR beam, there is practically no IR light at frequencies greater than 4000 cm^{-1} impinging on the crystal; however, infrared absorptions of HCl (~2895 cm^{-1}) can still be measured with this FTIR setup. As will be shown, with the 3861-cm^{-1} LPF in the IR beam, no measurable IR-induced reaction is observed.

The infrared spectrum of a 50-ppm Cl_2-doped pH_2 solid in the H_2 fundamental region (4100–5000 cm^{-1}) is shown in figure 9. The presence of Cl_2 can be detected in this region by the sharp Cl_2-induced $Q_1(0)$ absorption near 4150 cm^{-1}, which is labeled in figure 9. The intensity of this Cl_2-induced $Q_1(0)$ absorption feature is proportional to the Cl_2 concentration in the crystal. The Cl_2 dopant also produces a perturbed $S_1(0)$

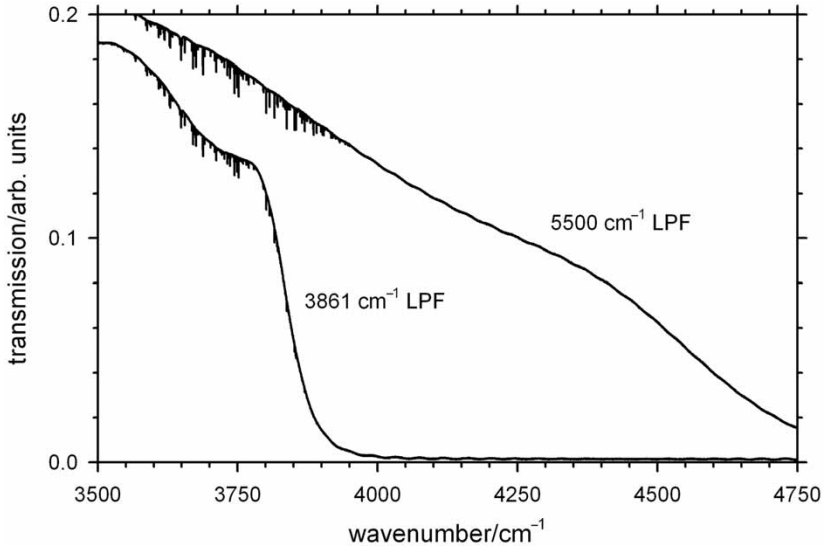

Figure 8. Transmission spectra from 3500 to 4750 cm^{-1} with no sample for the two longpass filters (LPF) used in this work. Each transmission profile is labeled by the corresponding LPF used in recording the transmission profile. Note there is practically no IR intensity above 4000 cm^{-1} with the 3861-cm^{-1} LPF. The sharp absorptions in each transmission profile are due to atmospheric H_2O absorptions.

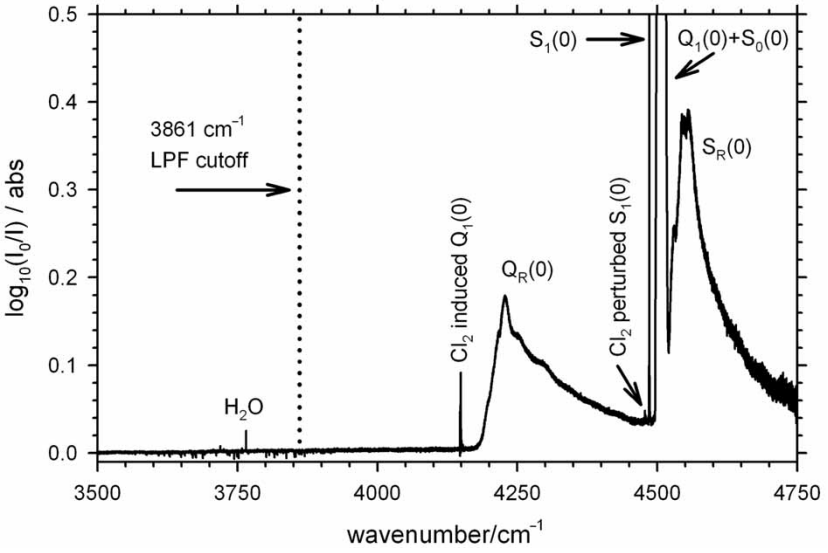

Figure 9. Infrared absorption spectrum of a 2.1(1)-mm thick 50 ppm Cl_2-doped pH_2 solid in the H_2 fundamental region recorded at 2.0 K. The presence of the Cl_2 dopant is evidenced by the induced $Q_1(0)$ absorption and the perturbed $S_1(0)$ absorption. The other solid pH_2 absorptions labeled in this region are well known. The frequency cutoff of the 3861-cm^{-1} LPF is shown as a dotted vertical line.

absorption just to the red of the IR-allowed $S_1(0)$ transition at 4485.9 cm^{-1}, characteristic of solid pH_2. The broad absorptions labeled $Q_R(0)$ and $S_R(0)$ are the phonon sidebands of the $Q_1(0)$ and $S_1(0)$ zero phonon lines, respectively. The $Q_1(0)+S_0(0)$ transition is a 'double' transition in which a pair of adjacent pH_2 molecules absorb a single IR photon resulting in pure rotational excitation of one pH_2 and pure vibrational excitation of the other. The $Q_R(0)$ and $Q_1(0)+S_0(0)$ pH_2 absorptions both result in the creation of delocalized $v=1$ vibrons. Note that all the absorptions of the pH_2 solid at frequencies greater than 4000 cm^{-1} in figure 9 are prevented when the 3861-cm^{-1} LPF is in the FTIR (figure 8).

Photolysis of Cl_2 at 355 nm has been well studied in the gas-phase both experimentally [68] and theoretically [69]. Photolysis at this wavelength is known to produce more than 99.4% of the nascent Cl atoms in their ground spin–orbit state ($Cl\ ^2P_{3/2}$) [68]. Conservation of energy dictates that:

$$E_T = \frac{m(Cl)}{m(Cl_2)}\left[E_{ph} - \Delta E_{SO} - D_0 + E_v(Cl_2) + E_{rot}(Cl_2)\right] \quad (4)$$

where E_T is the translational energy of the Cl atom, $E_{ph} = 28170\ cm^{-1}$ is the 355-nm photon energy, $\Delta E_{SO} = 882\ cm^{-1}$ is the gas phase Cl spin–orbit splitting [70], $D_0 = 19\,999\ cm^{-1}$ is the dissociation energy of Cl_2 ($X^1\Sigma_g$) [71], and $E_v(Cl_2)$ and $E_{rot}(Cl_2)$ are the vibrational and rotational energies of the Cl_2 parent molecule, which are both assumed to be zero in this case. According to equation (4), photodissociation of Cl_2 in solid pH_2 should result in ground spin–orbit state Cl atoms with

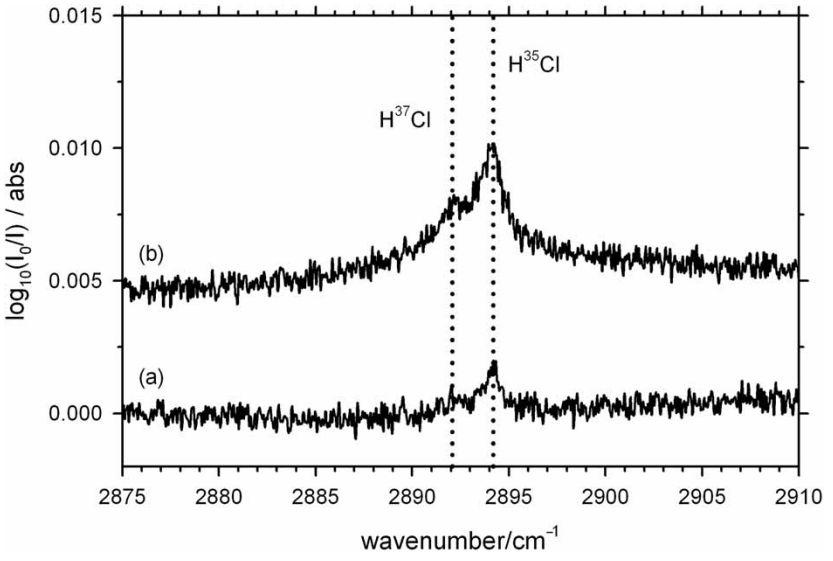

Figure 10. Infrared absorption spectra in the HCl $R_1(0)$ region for a 50-ppm Cl_2-doped pH_2 solid at 2.0 K. Trace (a) is the as-deposited sample before 355-nm photolysis and trace (b) is after 30 min of 10-Hz 355-nm photolysis at 1(0.5) mJ pulse^{-1}. The $R_1(0)$ infrared transition frequencies for the $H^{37}Cl$ and $H^{35}Cl$ isotopomers determined previously are shown as vertical dotted lines.

approximately 4086 cm^{-1} of translational energy. The translational energy of the nascent Cl atoms is more than twice the barrier to reaction ($E_a = 1720$ cm^{-1}) and, thus, the Cl atoms can react with the surrounding pH_2 matrix [66].

The extent of reaction will be monitored by measuring the absorption intensity of the $R_1(0)$ rovibrational transition of HCl. The infrared spectroscopy of HCl in solid pH_2 has been measured previously and HCl is found to undergo nearly free rotation [26]. Thus, at 2 K the only observable HCl rovibrational transition is the $R_1(0)$ transition out of the $J = 0$ ground rotational state. Figure 10 shows spectra of a 50-ppm Cl_2-doped pH_2 solid in the HCl $R_1(0)$ region before and after 355-nm photolysis. During photolysis the glowbar source was turned off and following photolysis the IR spectrum shown in figure 10 was recorded with the 3861 cm^{-1} LPF in the FTIR beam (*i.e.* no absorptions >4000 cm^{-1}). The small amount of HCl present before photolysis is presumably due to reactions of Cl_2 prior to the gas being incorporated into the pH_2 solid (*e.g.* reactions on the surface of the stainless steel tube used to introduce the Cl_2 gas into the cryostat). The HCl $R_1(0)$ feature does increase after 30 min of 355-nm photolysis at 2 K, but the increase is modest. This indicates that the overwhelming majority of photodissociation events are non-reactive. At these Cl_2 concentrations, 355-nm photodissociation efficiently leads to the production of trapped Cl atoms even though the nascent Cl atoms are produced with 4086 cm^{-1} kinetic energies. The lack of reaction induced by the 355-nm photodissociation of Cl_2 must be a result of the low reactivity of the $Cl + H_2(v = 0)$ system [72] and the high thermal conductivity [13] of solid pH_2, which very effectively dissipates the excess translational energy of the nascent Cl atoms, thereby, trapping the Cl atom below the barrier to reaction.

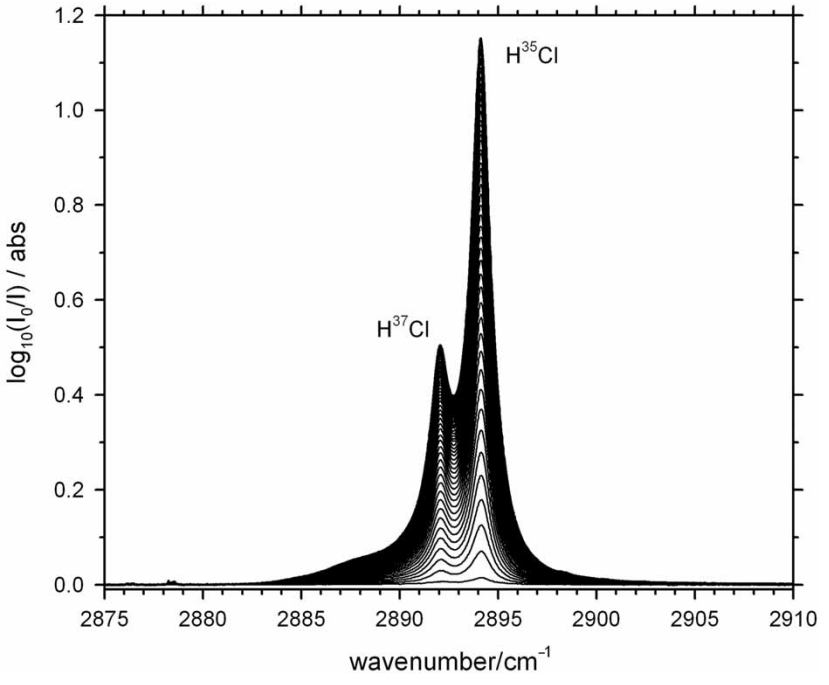

Figure 11. Infrared absorption spectra in the HCl $R_1(0)$ region recorded every 8 min with a collection time of 127 s for a Cl atom-doped pH_2 solid at 2.0 K being irradiated with IR light above 4000 cm^{-1}. The spectra are recorded with the 5500-cm^{-1} LPF in the IR beam and show the HCl $R_1(0)$ absorption increase to a maximum in the 528-min duration of the sequential scans.

Repeated scans with the 3861-cm^{-1} LPF in the beam show no change in the intensity of the HCl $R_1(0)$ absorption feature. However, if the 3861-cm^{-1} LPF is replaced with the 5500-cm^{-1} LPF, and IR light above 4000 cm^{-1} is allowed to irradiate the sample, the intensity of the HCl $R_1(0)$ feature is observed to steadily increase to a maximum value with time. Figure 11 shows a typical series of repeated scans recorded at 8-min intervals with the 5500-cm^{-1} LPF in the IR beam after 355-nm photolysis is complete. IR radiation at frequencies above 4000 cm^{-1} is inducing the reaction $Cl + H_2 \rightarrow HCl + H$.

The kinetics of the IR-induced reaction were measured by integrating the entire $R_1(0)$ absorption feature (both $H^{37}Cl$ and $H^{35}Cl$ isotopomers) shown in figure 11 from 2881 to 2910 cm^{-1} and plotting the integrated absorbance *versus* time. In this analysis, zero time is defined as the time when the 5500-cm^{-1} LPF filter is exchanged for the 3861-cm^{-1} LPF filter after UV photolysis is complete. The results of four separate kinetic experiments are plotted in figure 12. In each separate experiment, a 50-ppm Cl_2-doped pH_2 solid was irradiated with 355 nm light for 30 min. In the first control experiment, repeated scans are taken after 355-nm photolysis with the 3861-cm^{-1} LPF in the IR beam. As illustrated in figure 12, under these experimental conditions, no growth in the HCl $R_1(0)$ absorption is measured over a 500-min time range. In three other experiments, repeated scans with the 5500-cm^{-1} LPF in the IR beam were taken with three different intensities of IR light. The UV photolysis conditions for all four

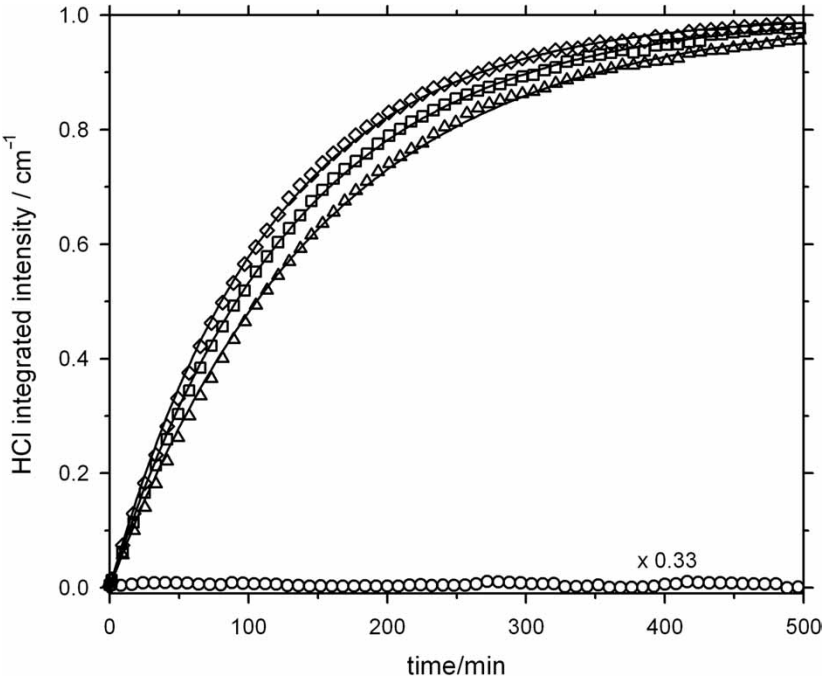

Figure 12. Plot of the HCl integrated intensity as a function of irradiation time with the FTIR glowbar source and 5500-cm^{-1} LPF. Four separate experiments are shown: circles are the control experiment conducted with the 3861-cm^{-1} LPF in the beam and an aperture size of 4.0 mm. The three other experiments utilized the 5500-cm^{-1} LPF: triangles are with a 2.5-mm aperture, squares are with a 3.15-mm aperture, and diamonds are with a 4.0-mm aperture. The three 5500-cm^{-1} LPF data have been normalized to one for ease of comparison and the intensity of the control experiment has been multiplied by a similar scaling factor. The lines represent fits of the data to equation (5). See text for details.

experiments were as nearly identical as experimentally could be achieved (50 ppm Cl_2 concentrations, 30 min, 1 mJ pulse^{-1} photolysis). The amount of IR light was crudely adjusted by changing the aperture size in the FTIR spectrometer. The aperture size changes not only the intensity of light but also the volume of the solid pH_2 sample that is irradiated with the IR light. The smaller the aperture, the less IR light illuminating the crystal as well as a smaller irradiation volume. Note that, as expected, increasing the size of the aperture speeds up the reaction rate in a systematic fashion.

The IR data presented in figure 12 could be well fit by a simple two parameter first-order rate equation:

$$I(t) = I(\infty)(1 - e^{-kt}) \tag{5}$$

where $I(t)$ is the integrated absorbance at time t, k is the first-order rate constant, t is the time after the reaction is initiated, and $I(\infty)$ is the integrated absorbance at infinite time. The fitted rate constants for the three experiments are reported in table 2. The reported error limits represent only the uncertainty of the fit.

Table 2. Fitted rate constants for the HCl $R_1(0)$ kinetic data measured with the 5500-cm^{-1} LPF in the IR beam.

Aperture diameter (mm)	k (min^{-1})
2.5	0.00655(5)
3.15	0.00759(3)
4.0	0.00861(5)

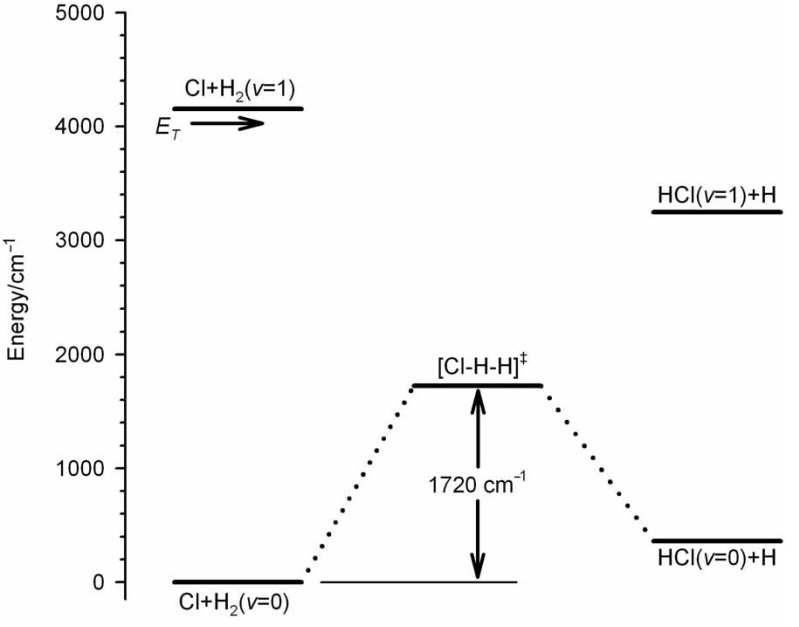

Figure 13. Energy level and correlation diagram for the $Cl+H_2 \rightarrow HCl + H$ reaction. The effective ground state potential for ground spin–orbit state Cl reacting with ground vibrational and rotational state $H_2(v=0, j=0)$ has a reaction barrier of 1720 cm^{-1} and is endothermic by 360 cm^{-1}. The energies of the asymptotic $H_2(v=1)$ and $HCl(v=1)$ excited vibrational states are shown. The translational energy of the nascent Cl photofragments following 355-nm photolysis is indicated by the arrow label E_T.

The observed IR dependence of the reaction of Cl atoms with the pH_2 matrix can be rationalized through an examination of the reactive potential energy surface, which is illustrated in figure 13. After the excess translational energy of the photoejected Cl atom is dissipated by the pH_2 solid, reaction (2) can not proceed even *via* quantum mechanical tunneling because the reaction is endothermic by 360 cm^{-1}. At 2 K, the available thermal energy ($kT \approx 1.4\,cm^{-1}$) is more than two orders of magnitude smaller than the endothermicity of the reaction and, thus, the reaction rate is near zero. Given the high vibrational frequency of H_2, thermal population of excited H_2 vibrational states in the solid is also exceedingly low. However, solid pH_2 absorbs near IR radiation in a window between 4000 and 5000 cm^{-1} that produces vibrationally excited $H_2(v=1)$.

As indicated in figure 13, reaction (3) of $Cl + H_2(v = 1)$ is exoergic and, thus, possible at temperatures of 2 K.

There are several plausible photochemical mechanisms by which IR absorptions in the region between 4000 and 5000 cm^{-1} can induce reaction. One mechanism relies on the presence of the Cl atom to induce the pure vibrational $Q_1(0)$ infrared absorption in the pH_2 solid. The ability of atomic dopants to induce the $Q_1(0)$ absorption is well documented [27, 58] and was discussed in detail for Rg atoms in section 4. This absorption corresponds to vibrational excitation of pH_2 molecules in the first solvation shell of the Cl atom and, thus, should readily result in reaction since the vibrationally excited H_2 molecules are in direct contact with the Cl atom. Another possible mechanism involves IR absorptions of the pH_2 solid itself and the creation of delocalized vibrons, which can travel through the solid and scatter off trapped Cl atoms inducing reaction. For example, the broad $Q_R(0)$ phonon sideband absorption results in the creation of vibrons and phonons within solid pH_2. Vibrons are also created by the $Q_1(0) + S_0(0)$ cooperative transition, which is approximately 25 cm^{-1} broad and has a strong absorption strength.

We speculate the vibron mechanism dominates under these experimental conditions of broadband IR irradiation because pH_2 absorptions that lead to the formation of vibrons are much broader than the sharp Cl atom induced $Q_1(0)$ absorption. The broad pH_2 absorptions are better matched to the broadband IR source and, thus, couple more IR radiation into the solid creating greater concentrations of $H_2(v = 1)$. Possible candidates are the $Q_R(0)$ or $Q_1(0) + S_0(0)$ transitions because both of these absorptions create delocalized vibrons and have large integrated intensities. However, if the vibron mechanism is operative under these conditions, what is not fully understood is how the vibron will interact with the Cl atoms, since the presence of the Cl atom shifts the vibrational frequency of neighboring pH_2 molecules. The shift in the pH_2 vibrational frequency induced by the Cl atom may make the amplitude of the delocalized vibron on these pH_2 molecules very small. Furthermore, some of the other pH_2 absorptions in this region may also contribute to IR-induced reaction. However, absorptions that result in rovibrational excitation (*e.g.* $S_1(0)$ or $S_R(0)$) are not suspected to make a significant contribution because rovibrational excitations are less mobile since the coupling terms involving transfer of both vibration and rotation are much smaller than the pure vibrational coupling terms. The present interpretation, that the vibron mechanism dominates under these conditions, is clearly speculative and more work is necessary to discern the important photochemical pathways for the IR-induced reaction kinetics reported in this study.

Regardless of the specifics of the photochemical mechanism, the simple first-order kinetics is consistent with the reaction of Cl with vibrationally excited H_2. Specifically, the change in HCl concentration as a function of time can be expressed as:

$$\frac{d[HCl]}{dt} = k[H_2(v = 1)][Cl] = k_{ef}[Cl] \tag{6}$$

When the solid is being irradiated by light above 4000 cm^{-1}, vibrationally excited H_2 is constantly being created (absorption) and destroyed (reaction and/or relaxation) within the solid and the $H_2(v = 1)$ concentration becomes effectively constant. Under these

conditions, the rate law simplifies to the effective first-order rate law given in equation (6). When the sample is not being irradiated by IR light above 4000 cm^{-1}, the $H_2(v=1)$ concentration is effectively zero and the rate of reaction is negligible. Similarly, if the intensity of the IR light is increased, the concentration of $H_2(v=1)$ increases accordingly and a larger effective rate constant is measured.

The contribution of other reactions to the formation of HCl needs to also be considered. The other product of reaction (3) is the H atom. While the diffusion rates of Cl or HCl at these temperatures are very low, the H atom is known to be mobile in solid pH_2 *via* the $H + H_2$ exchange reaction [73]. The H atom could react *via* a tunneling mechanism with either Cl or unphotodissociated Cl_2 to produce HCl since both of these reactions are exothermic. At high HCl concentrations, the H atom might also start to contribute to back reaction. Unfortunately, there is no detection scheme using FTIR spectroscopy that can be used to detect the presence of H atoms in solid pH_2. Nonetheless, work is underway to determine the importance of H atom reactions under these experimental conditions.

6. Concluding remarks

This review article surveys recent work from this laboratory on the infrared spectroscopy of chemically doped pH_2 solids. Progress is being made in the synthesis and characterization of chemically doped pH_2 solids using infrared spectroscopy; however, there are still many questions that await further study and new chemical systems to be explored. It is hoped that the information presented in this article will be used by researchers to better design experiments to utilize solid pH_2 as a condensed phase environment for chemical studies. The infrared-induced Cl atom reactions reported in this article are the first step from this laboratory in this direction.

Acknowledgments

The authors would like to acknowledge the valuable contribution of Britney D. Lorenz to the experimental work on N_2O hydrogen clusters described in this review article. We would also like to thank Mario E. Fajardo and Robert J. Hinde for insightful discussions on all the topics covered in this review. The ultraviolet laser system used in the photochemical studies was purchased with funds from an equipment grant from the United States Air Force Office of Scientific Research. This research has been supported by a grant from the Petroleum Research Fund, administered by the American Chemical Society, an award from the Research Corporation, and by a grant from Chemistry Division of the National Science Foundation (Grant No. CHE-03–16268).

References

[1] J. Van Kranendonk, Physica **25,** 1080 (1959).
[2] J. Van Kranendonk, Can. J. Phys. **38,** 240 (1960).
[3] J. Van Kranendonk and G. Karl, Rev. Mod. Phys. **40,** 531 (1968).
[4] E. J. Allin, W. F. J. Hare, and R. E. MacDonald, Phys. Rev. **98,** 554 (1955).

[5] W. F. J. Hare, E. J. Allin, and H. L. Welsh, Phys. Rev. **99,** 1887 (1955).
[6] H. P. Gush, W. F. J. Hare, E. J. Allin, and H. L. Welsh, Phys. Rev. **106,** 1101 (1957).
[7] H. J. Allin, H. P. Gush, W. F. J. Hare, and H. L. Welsh, Nuovo Cimento Suppl. **9,** 77 (1958).
[8] H. P. Gush, W. F. J. Hare, E. J. Allin, and H. L. Welsh, Can. J. Phys. **38,** 176 (1960).
[9] A. Farkas, *Orthohydrogen, Parahydrogen and Heavy Hydrogen* (Cambridge University Press, 1935).
[10] J. Van Kranendonk, *Solid Hydrogen:- Theory of the Properties of Solid H_2, HD, and D_2* ([Plenum Press, New York, 1983).
[11] P. C. Souers, *Hydrogen Properties for Fusion Energy* (University of California Press, Berkeley, 1986).
[12] B. I. Verkin, *Handbook of Properties of Condensed Phases of Hydrogen and Oxygen* (Hemisphere Publishing, New York, 1991).
[13] I. F. Silvera, Rev. Mod. Phys. **52,** 393 (1980).
[14] T. Oka, Annu. Rev. Phys. Chem. **44,** 299 (1993).
[15] T. Momose, M. Fushitani, and H. Hoshina, Int. Rev. Phys. Chem. **24,** 533 (2005).
[16] T. Momose and T. Shida, Bull. Chem. Soc. Jpn **71,** 1 (1998).
[17] M. E. Fajardo and S. Tam, J. Chem. Phys. **108,** 4237 (1998).
[18] S. Tam and M. E. Fajardo, Rev. Sci. Instrum. **70,** 1926 (1999).
[19] Y.-J. Wu, X. Yang, and Y.-P. Lee, J. Chem. Phys. **120,** 1168 (2004).
[20] Y.-P. Lee, Y.-J. Wu, R. M. Lees, L.-H. Xu, and J. T. Hougen, Science **311,** 365 (2006).
[21] L. Andrews and X. Wang, Rev. Sci. Instrum. **75,** 3039 (2004).
[22] J. Ceponkus and B. Nelander, J. Chem. Phys. **124,** 024504 (2006).
[23] K. Yoshioka and D. T. Anderson, J. Chem. Phys. **119,** 4731 (2003).
[24] K. Yoshioka and D. T. Anderson, J. Mol. Struct. **786,** 123 (2006).
[25] S. Tam and M. E. Fajardo, Appl. Spectrosc. **55,** 1634 (2001).
[26] D. T. Anderson , R. J. Hinde, S. Tam, and M. E. Fajardo, J. Chem. Phys. **116,** 594 (2002).
[27] R. J. Hinde, D. T. Anderson, S. Tam, and M. E. Fajardo, Chem. Phys. Lett. **356,** 355 (2002).
[28] S. Tam, M. E. Fajardo, H. Katsuki, H. Hoshina, T. Wakabayashi, *et al.*, J. Chem. Phys. **111,** 4191 (1999).
[29] R. Oyarzun and J. Van Kranendonk, Can. J. Phys. **50,** 1494 (1972).
[30] S. A. Boggs and H. L. Welsh, Can. J. Phys. **51,** 1910 (1973).
[31] B. J. Roffey, S. A. Boggs, and H. L. Welsh, Can. J. Phys. **52,** 2451 (1974).
[32] D. Zhou, C. M. Edwards, and N. S. Sullivan, Phys. Rev. Lett. **62,** 1528 (1989).
[33] A. E. Meyerovich, Phys. Rev. B **42,** 6068 (1990).
[34] H. Meyer, J. Low-Temp. Phys. **24,** 381 (1998).
[35] S. M. Freund, G. Duxbury, M. Romheld, J. T. Tiedje, and T. Oka, J. Mol. Spectrosc. **52,** 38 (1974).
[36] S. Tam and M. E. Fajardo, Fiz. Nizk. Temp. **26,** 889 (2000).
[37] M. E. Fajardo and S. Tam, J. Chem. Phys. **115,** 6807 (2001).
[38] M. E. Fajardo, S. Tam, and M. E. DeRose, J. Mol. Struct. **695/696,** 111 (2004).
[39] J. Tang and A. R. W. McKellar, J. Chem. Phys. **117,** 8308 (2002).
[40] J. Tang and A. R. W. McKellar, J. Chem. Phys. **123,** 114314 (2004).
[41] Y. Xu, W. Jäger, J. Tang, and A. R. W. McKellar, Phys. Rev. Lett. **91,** 163401 (2003).
[42] J. P. Toennies and A. F. Vilesov, Annu. Rev. Phys. Chem. **49,** 1 (1998).
[43] C. Callegari, K. K. Lehmann, R. Schmied, and G. Scoles, J. Chem. Phys. **115,** 10090 (2001).
[44] B.D. Lorenz and D. T. Anderson (to be submitted).
[45] E. L. Knuth, F. Schunemann, and J. P. Toennies, J. Chem. Phys. **102,** 6258 (1995).
[46] S. Grebenev, B. Sartakov, J. P. Toennies, and A. F. Vilesov, Science **289,** 1532 (2000).
[47] S. Grebenev, B. Sartakov, J. P. Toennies, and A. Vilesov, Phys. Rev. Lett. **89,** 225301 (2002).
[48] P. Sindzingre, D. M. Ceperley, and M. L. Klein, Phys. Rev. Lett. **67,** 1871 (1991).
[49] K. Kinugawa, P. B. Moore, and M. L. Klein, J. Chem. Phys. **106,** 1154 (1997).
[50] Y. Kwon and K. B. Whaley, **89**, 273401 (2002).
[51] D. T. Moore, M. Ishiguro, and R. E. Miller, J. Chem. Phys. **115,** 5144 (2001).
[52] D. T. Moore and R. E. Miller, J. Phys. Chem A **107,** 10805 (2003).
[53] D. T. Moore and R. E. Miller, J. Chem. Phys. **118,** 9629 (2003).
[54] D. T. Moore and R. E. Miller, J. Chem. Phys. **119,** 4713 (2003).
[55] D. T. Moore and R. E. Miller, J. Phys. Chem. A **108,** 1930 (2004).
[56] F. Schmidt, Phys. Rev. B **10,** 4480 (1974).
[57] V. Shevtsov, E. Ylinen, P. Malmi, and M. Punkkinen, Phys. Rev. B **62,** 12386 (2000).
[58] R. J. Hinde, J. Chem. Phys. **119,** 1 (2003).
[59] P. Raston and D. T. Anderson (to be submitted).
[60] R. J. Le Roy and J. Van Kranendonk, J. Chem. Phys. **61,** 4750 (1974).
[61] R. J. Le Roy and J. M. Hutson, J. Chem. Phys. **86,** 837 (1987).
[62] V. F. Sears and J. Van Kranendonk, Can. J. Phys. **42,** 980 (1964).
[63] A. R. W. McKellar and H. L. Welsh, J. Chem. Phys. **55,** 595 (1971).

[64] A. R. W. McKellar and H. L. Welsh, Can. J. Phys. **50,** 1458 (1972).
[65] H. P. Gush and J. Van Kranendonk, Can. J. Phys. **40,** 1461 (1962).
[66] M. Alagia, N. Balucani, L. Cartechini, P. Casavecchia, G. G. Volpi, *et al.*, Phys. Chem. Chem. Phys. **2,** 599 (2000).
[67] J. C. Polanyi, Acc. Chem. Res. **5,** 161 (1972).
[68] P. C. Samartzis, B. L. G. Bakker, T. P. Rakitzis, D. H. Parker, and T. N. Kitsopoulos, J. Chem. Phys. **110,** 5201 (1999).
[69] D. B. Kokh, A. B. Alekseyev, and R. J. Buenker, J. Chem. Phys. **120,** 11549 (2004).
[70] E. Tiemann, H. Kanamori, and E. Hirota, J. Chem. Phys. **88,** 2457 (1988).
[71] R. J. Le Roy and R. B. Bernstein, J. Mol. Spectrosc. **37,** 109 (1971).
[72] S. S. Kumaran, K. P. Lim, and J. V. Michael, J. Chem. Phys. **101,** 9487 (1994).
[73] S. Miyazaki, S. Mori, T. Nagasaka, J. Kumagai, Y. Aratono, *et al.*, J. Phys. Chem. A **104,** 9403 (2000).